# Schisandrin B exhibits anti-proliferative effects by inducing ferroptosis in pancreatic cancer

FENGJIN LI[1*], JIACAI FU[2*], XIAOWEI LIN[1*], YANTING LIU[1], LU YANG[1], YUXIN LI[1], TIELI PENG[1] and LING QI[1]

[1]Institute of Digestive Diseases, The Affiliated Qingyuan Hospital (Qingyuan People's Hospital), Guangzhou Medical University, Qingyuan, Guangdong 511518, P.R. China; [2]Department of Pharmacy, West China Hospital, Sichuan University, Chengdu, Sichuan 610047, P.R. China

Received January 17, 2026; Accepted May 15, 2026

DOI: 10.3892/or.2026.9152

**Abstract.** Pancreatic cancer (PC) is a lethal malignant tumor of the digestive system with a low survival rate. Current therapies provide only modest benefits for patients and new therapeutic options are urgently needed. Schisandrin B (Sch B) has demonstrated novel antitumor activity in several preclinical models; however, its effects on PC remain unclear. In the present study, the anti-proliferative effects of Sch B *in vitro* were evaluated in PC cell lines. The underlying molecular mechanisms were explored using RNA sequencing, drug affinity responsive target stability (DARTS), molecular docking and small interfering RNA transfection. The antitumor effects of Sch B *in vivo* were evaluated using both a subcutaneous xenograft mouse model and an orthotopic genetically engineered mouse model. The *in vitro* studies showed that Sch B significantly inhibited the proliferation of PC cells and induced cell death in a dose-dependent manner. Mechanistically, transcriptome Kyoto Encyclopedia of Genes and Genomes enrichment analysis revealed that differentially expressed genes were significantly enriched in the 'ferroptosis' signaling pathway. Sch B triggered ferroptosis by promoting iron overload, lipid peroxidation and glutathione (GSH) depletion, as well as regulating the expression of ferroptosis-related proteins [including GSH peroxidase 4, solute carrier family 3 member 2, acyl-CoA synthetase long-chain family member 4 (ACSL4), γ-glutamyl-cysteine ligase catalytic subunit and GSH synthetase]. Furthermore, pre-treatment with the ferroptosis inhibitor ferrostatin-1 partially reversed the anti-proliferative effects and ferroptosis-related events induced by Sch B. DARTS assays and molecular docking analyses confirmed the direct interaction between Sch B and ACSL4. Notably, silencing ACSL4 expression also partially reversed the anti-proliferative effects and ferroptosis-related events induced by Sch B. The *in vivo* studies demonstrated that Sch B suppressed tumor growth in subcutaneous xenograft models with good biosafety, and inhibited metastasis in orthotopic genetically engineered mice. In conclusion, Sch B may exert anti-proliferative effects at least partially by inducing ACSL4-dependent ferroptosis in PC.

*Correspondence to:* Professor Ling Qi or Professor Tieli Peng, Institute of Digestive Diseases, The Affiliated Qingyuan Hospital (Qingyuan People's Hospital), Guangzhou Medical University, 35 Yinquan North Road, Qingcheng, Qingyuan, Guangdong 511518, P.R. China
E-mail: qiling1718@gzhmu.edu.cn
E-mail: pengtl@163.com

*Contributed equally

*Abbreviations:* PC, pancreatic cancer; Sch B, Schisandrin B; CCK-8, Cell Counting Kit-8; $IC_{50}$, half maximal inhibitory concentration; Fer-1, ferrostatin-1; DFO, deferoxamine mesylate; NAC, N-acetylcysteine; NEC-1, necrostatin-1; MDA, malondialdehyde; GSH, glutathione; TF, transferrin; ACSL4, acyl-CoA synthetase long-chain family member 4; GCLC, γ-glutamyl-cysteine ligase catalytic subunit; GSS, glutathione synthetase; GPX4, glutathione peroxidase 4; SLC3A2, solute carrier family 3 member 2; SLC7A11, solute carrier family 7 member 11; DEGs, differentially expressed genes; DARTS, drug affinity responsive target stability; ALT, alanine aminotransferase; AST, aspartate aminotransferase; CK, creatine kinase; LDH, lactate dehydrogenase; CREA, creatinine; UA, uric acid

*Key words:* Sch B, cell proliferation, ferroptosis, pancreatic cancer, acyl-CoA synthetase long-chain family member 4

## Introduction

Pancreatic cancer (PC) is the third leading cause of cancer-associated mortality in the United States and the sixth in China, and it is projected to become the second in the United States by 2030 (1,2). Due to late diagnosis, early metastasis and poor prognosis, the overall 5-year survival rate for PC is <13% (3). Surgical resection combined with systemic chemotherapy remains the only curative option or possibility with a chance of long-term survival, but most patients are ineligible due to presenting with locally advanced disease or distant metastasis at the time of initial diagnosis (4-6). FOLFIRINOX and gemcitabine-based therapies have only modestly improved overall survival, and their efficacy is limited by multidrug resistance and systemic toxicities (7,8). Thus, new therapeutic strategies are urgently needed. Recent advances include gene

therapy, molecular targeted therapy, cellular immunotherapy and natural compounds, all of which highlight the growing interest in innovative PC treatments (9-13).

Ferroptosis is an iron-dependent form of programmed cell death (PCD) characterized by distinct morphological, biochemical and genetic features that differentiate it from other types of cell death, including apoptosis, pyroptosis, autophagy and necroptosis (14). The primary hallmarks of ferroptosis are the accumulation of iron and lipid peroxides (15). PC cells exhibit reprogrammed organelle functions, resulting in increased iron availability and reactive oxygen species (ROS) production compared with normal cells; this alteration enhances the intrinsic vulnerability of these cells to ferroptotic cell death (16). Ferroptosis inducers have shown considerable potential as innovative therapeutic strategies for inhibiting tumor growth, enhancing the efficacy of conventional antitumor agents, and overcoming drug resistance to systemic therapy, radiotherapy and immunotherapy (17-20). These observations suggest that inducing ferroptosis is a promising therapeutic strategy for PC.

*Schisandra chinensis* (Turcz.) Baill., known as Wu Wei Zi in Chinese, is a medicinal and edible herb, which is widely used in traditional Chinese formulations documented in the Chinese Pharmacopoeia (21). Schisandrin B (Sch B) is one of the most abundant dibenzocyclooctadiene lignans in *S. chinensis* fruits, which exhibits various beneficial properties, including antitumor, anti-inflammatory, hepatoprotective, cardioprotective and neuroprotective effects (22-26). Previous studies have shown that Sch B exerts antitumor effects by inducing apoptosis, pyroptosis, autophagy and ROS production in human cancer (27-29). Additionally, Sch B has synergistic effects with conventional or targeted antitumor agents, enhancing clinical efficacy and reducing adverse effects (30-33). These organ-protective and antitumor properties suggest that Sch B may be a valuable adjunctive treatment for PC; however, whether Sch B can trigger ferroptosis in PC and its mechanism remain unclear. The present study aimed to investigate the anti-proliferative effects and mechanisms of Sch B against PC *in vitro* and *in vivo*.

## Materials and methods

*Chemicals and antibodies*. Sch B (cat. no. B21327-1g) was purchased from Shanghai Yuanye Bio-Technology Co., Ltd. Sch B was prepared as a 125 mM stock solution in 100% DMSO [the final concentration of DMSO in culture medium did not exceed 0.1% (v/v)] and stored in the dark at -20˚C in our laboratory. Ferrostatin-1 (Fer-1; cat. no. HY-100579), deferoxamine mesylate (DFO; cat. no. HY-B1625), Z-VAD-FMK (cat. no. HY-16658B), N-acetylcysteine (NAC; cat. no. HY-B0215) and necrostatin-1 (NEC-1; cat. no. HY-15760) were purchased from MedChemExpress. Anti-acyl-CoA synthetase long-chain family member 4 (ACSL4; cat. no. 22401-1-AP), anti-GSH synthetase (GSS; cat. no. 67598-1-Ig) anti-solute carrier family 3 member 2 (SLC3A2; cat. no. 15193-1-AP), anti-transferrin (TF; cat. no. 17435-1-AP), and anti-α-tubulin (cat. no. 66031-1-Ig) were purchased from Proteintech Group, Inc. Anti-glutathione (GSH) peroxidase 4 (GPX4; cat. no. ab125066), anti-γ-glutamyl-cysteine ligase catalytic subunit (GCLC; cat. no. ab207777), anti-solute carrier family 7 member 11 (SLC7A11; cat. no. ab307601) and anti-Ki67 (cat. no. ab16667) were purchased from Abcam.

*Cell culture*. Human pancreatic ductal adenocarcinoma cell lines MIA PaCa-2 (cat. no. CRL-1420), PANC-1 (cat. no. CRL-1469) and PL45 (cat. no. CRL-2558) were purchased from American Type Culture Collection. These cell lines were cultured in DMEM (cat. no. C11995500BT; Gibco; Thermo Fisher Scientific, Inc.) supplemented with 1% penicillin-streptomycin (PS; cat. no. 15140122; Gibco; Thermo Fisher Scientific, Inc.) and 10% fetal bovine serum (FBS; cat. no. FSP500; Shanghai ExCell Biology, Inc.). Human pancreatic duct epithelial cells (hTERT-HPNE) were purchased from Guangzhou Jennio Biotechnology Co., Ltd. and cultured in RPMI-1640 medium (cat. no. C11875500BT; Gibco; Thermo Fisher Scientific, Inc.) supplemented with 1% PS and 10% FBS. All cells were maintained at 37˚C with 5% $CO_2$ in a sterile incubator. All cell lines tested negative for mycoplasma using the Mycoplasma test kit (cat. no. G1901; Wuhan Servicebio Technology Co., Ltd.).

*Cell viability assay*. MIA PaCa-2, PANC-1, PL45 and hTERT-HPNE cells were seeded in 96-well plates at a density of $3x10^3$ cells/well and incubated overnight. The cells were then treated with Sch B at concentrations of 0, 7.8, 15.6, 31.3, 62.5 or 125 $\mu$M for 24, 48 or 72 h at 37˚C. The control groups received an equivalent concentration of DMSO (≤0.1%). For inhibitor studies, the cells were pre-treated with Fer-1 (10 $\mu$M), DFO (20 $\mu$M), Z-VAD-FMK (50 $\mu$M), NEC-1 (50 $\mu$M) or NAC (2 mM) for 4 h at 37˚C, followed by treatment with Sch B (20 $\mu$M) for 24 h at 37˚C. Subsequently, 10 $\mu$l Cell Counting Kit-8 (CCK-8) reagent (cat. no. CK04; Dojindo Laboratories, Inc.) dissolved in 100 $\mu$l fresh medium was added to each well and incubated for 2 h. Absorbance was measured at 450 nm using a microplate reader (Tecan Group, Ltd.).

*Colony formation assay*. MIA PaCa-2 and PANC-1 cells were seeded in 6-well plates at a density of $1x10^3$ cells/well and incubated overnight. The cells were then treated with Sch B (5, 10 or 20 $\mu$M) or vehicle control (<0.1% DMSO) for 24 h at 37˚C. Subsequently, the cells were cultured for 10 days, with the medium changed every 3 days. Colonies were then fixed in 4% paraformaldehyde for 10 min at room temperature and stained with 0.1% crystal violet for 15 min at room temperature, after which, images were captured under an inverted light microscope (Zeiss AG). A colony was defined as a cluster of ≥50 cells and the number of colonies was semi-quantified using ImageJ version 1.4.3 software (National Institute of Health).

*EdU assay*. MIA PaCa-2 and PANC-1 cells were seeded in 8-well chamber slides at a density of $9x10^3$ cells/well and were incubated overnight. The cells were then treated with Sch B (5, 10 or 20 $\mu$M) or vehicle control (<0.1% DMSO) for 24 h at 37˚C. For inhibitor experiments, the cells were pre-treated with Fer-1 (10 $\mu$M) for 4 h followed by treatment with Sch B (20 $\mu$M) for 24 h at 37˚C. Subsequently, 500 $\mu$l EdU working solution (cat. no. C10310; Guangzhou RiboBio Co., Ltd.) was added to each well and incubated for 2 h at 37˚C. The cells were then permeabilized with 0.5% Triton X-100 for 15 min at room temperature and were stained with Apollo 567 for 30 min

at room temperature. After washing, the slides were mounted with DAPI-containing Fluoroshield (cat. no. ab104139; Abcam). Images of EdU-positive cells were captured using a confocal microscope (Zeiss AG).

*Lactate dehydrogenase (LDH) release measurement*. Cell death was measured using the LDH cytotoxicity assay kit (cat. no. C0017; Beyotime Biotechnology). MIA PaCa-2 and PANC-1 cells were seeded in 35-mm dishes at a density of $9x10^4$ cells/dish and incubated overnight. The cells were then treated with Sch B (5, 10 or 20 $\mu$M) or vehicle control (<0.1% DMSO) for 24 h at 37˚C. For inhibitor experiments, the cells were pre-treated with Fer-1 (10 $\mu$M) for 4 h followed by treatment with Sch B (20 $\mu$M) for 24 h at 37˚C. After treatment, the culture medium was collected and centrifuged at 800 x g for 5 min at 4˚C to remove cell debris. Subsequently, 120 $\mu$l cell culture supernatants were transferred to a new 96-well plate and mixed with 60 $\mu$l LDH working solution. After incubation for 30 min at 37˚C in the dark, the absorbance was measured at 490 nm using a microplate reader. The percentage of cell death was calculated as follows: (treated cell LDH-control cell LDH)/(maximum LDH release-control cell LDH) x100.

*Trypan blue staining*. The Trypan blue assay (cat. no. C0040; Beijing Solarbio Science & Technology Co., Ltd.) was performed to confirm the results of the LDH assay. MIA PaCa-2 and PANC-1 cells were seeded in 35-mm dishes at a density of $9x10^4$ cells/dish and incubated overnight. The cells were then treated with Sch B (5, 10 or 20 $\mu$M) or vehicle control (<0.1% DMSO) for 24 h at 37˚C. Subsequently, the cells were stained with 0.04% Trypan blue solution for 3 min at room temperature. The unstained (viable) and blue-stained (dead) cells were counted using an automatic cell counter (Guangzhou BodBoge Technology Co., Ltd.) and the percentage of dead cells was calculated.

*Detection of intracellular iron*. Intracellular $Fe^{2+}$ levels were measured using the FerroOrange fluorescent probe (cat. no. F374; Dojindo Laboratories, Inc.). MIA PaCa-2 and PANC-1 cells were seeded in 8-well chamber slides at a density of $9x10^3$ cells/well and incubated overnight. The cells were then treated with Sch B (5, 10 or 20 $\mu$M) or vehicle control (<0.1% DMSO) for 24 h at 37˚C. For inhibitor experiments, the cells were pre-treated with Fer-1 (10 $\mu$M) for 4 h followed by treatment with Sch B (20 $\mu$M) for 24 h at 37˚C. Subsequently, the cells were stained with 1 $\mu$M FerroOrange in serum-free medium for 30 min at 37˚C in the dark. Fluorescence intensity was acquired using a confocal microscope.

*Transmission electronic microscopy*. MIA PaCa-2 and PANC-1 cells were seeded in 150-mm dishes at a density of $6x10^5$ cells/dish and incubated overnight. The cells were then treated with Sch B (20 $\mu$M) or vehicle control (<0.1% DMSO) for 24 h at 37˚C. Subsequently, the cells were harvested and fixed in a 2.5% glutaraldehyde solution (pH 7.4) for 6 h at 4˚C. After washing with 0.1 M phosphate buffer (pH 7.2), the samples were postfixed with 1% $OsO_4$ for 4 h at 4˚C. Following dehydration, the samples were embedded in Epon-Araldite resin and polymerized at 60˚C for 48 h. Semithin sections (1 $\mu$m) were stained with toluidine blue for positioning, after which, ultrathin sections (70 nm) were collected on copper grids, stained with 2% uranyl acetate for 8 min at room temperature, followed by 2.7% lead citrate for 8 min at room temperature, and examined under a transmission electron microscope (Thermo Fisher Scientific, Inc.).

*Measurement of GSH and malondialdehyde (MDA) content*. The levels of GSH and MDA were measured using ELISA kits (cat. nos. S0052 and S0131S; Beyotime Biotechnology, Inc.) according to the manufacturer's protocol. MIA PaCa-2 and PANC-1 cells were seeded in 150-mm dishes at a density of $6x10^5$ cells/dish and incubated overnight. The cells were then treated with Sch B (5, 10 or 20 $\mu$M) or vehicle control (<0.1% DMSO) for 24 h at 37˚C. For inhibitor experiments, the cells were pre-treated with Fer-1 (10 $\mu$M) for 4 h followed by treatment with Sch B (20 $\mu$M) for 24 h at 37˚C. GSH and MDA levels in cell lysates were measured using a microplate reader.

*Determination of lipid peroxidation*. Lipid peroxidation was assessed using the C11-BODIPY (581/591) assay (cat. no. L267; Dojindo Laboratories, Inc.). MIA PaCa-2 and PANC-1 cells were seeded in 8-well chamber slides at a density of $9x10^3$ cells/well and incubated overnight. The cells were then treated with Sch B (5, 10 or 20 $\mu$M) or vehicle control (<0.1% DMSO) for 24 h at 37˚C. For inhibitor experiments, the cells were pre-treated with Fer-1 (10 $\mu$M) for 4 h followed by treatment with Sch B (20 $\mu$M) for 24 h at 37˚C. Subsequently, the cells were incubated with 2 $\mu$M C11-BODIPY (581/591) solution for 30 min at 37˚C. Fluorescence intensity was measured using a confocal microscope.

*Drug affinity responsive target stability (DARTS) analysis*. PANC-1 cells were treated with Sch B (20 $\mu$M) or vehicle control (<0.1% DMSO) for 24 h at 37˚C and then lysed using M-PER mammalian protein extraction reagent (cat. no. 78505; Thermo Fisher Scientific, Inc.) with protease inhibitor cocktail (cat. no. HY-K0010; MedChemExpress) on ice for 10 min. The lysates were centrifuged at 12,000 x g for 20 min at 4˚C, after which, the supernatants were collected and mixed with 10X TNC buffer (500 mM Tris-HCl, pH 8.0; 500 mM $CaCl_2$; 100 mM NaCl). Protein concentration was then quantified using a BCA assay. The lysates (4 $\mu$g/$\mu$l) in 1X TNC buffer were digested with pronase (0.25 $\mu$g/$\mu$l; cat. no. 63163824; Roche) at a pronase/protein ratio of 1:200 for 30 min at room temperature and the reaction was terminated by adding 5X SDS-PAGE loading buffer. Subsequently, the proteins were separated by SDS-PAGE and visualized by Coomassie staining; specific protein bands were excised for label-free liquid chromatography-tandem mass spectrometry (LC-MS/MS) analysis.

*LC-MS/MS analysis*. Nanoflow LC-MS/MS analysis of peptides was performed using a quadrupole Orbitrap Exploris™ 480 Mass Spectrometer (Thermo Fisher Scientific, Inc.) equipped with an EASY nLC 1200 ultra-high pressure system (Thermo Fisher Scientific, Inc.) via a nano-electrospray ion source. Briefly, peptides (500 ng) were loaded on a 25-cm column (150 $\mu$m inner diameter, packed with ReproSil-Pur C18-AQ 1.9-$\mu$m silica beads; Guangzhou Promegene Biotechnology Co., Ltd.). The peptides were eluted over a 60-min gradient

at a flow rate of 600 nl/min using buffer B (80% acetonitrile, 0.1% formic acid) as follows: 8-12% B for 5 min, 12-30% B for 30 min, 30-40% B for 9 min, 40-95% B for 1 min, followed by incubation with 95% B for 15 min.

The mass spectrometer was operated in positive ion mode with the FAIMS Pro™ Interface (Thermo Fisher Scientific, Inc.) cycling between compensation voltages of-45 V and -65 V every 1 sec. Full-scan MS spectra (350-1,200 m/z, 120,000 resolution) were acquired in the Orbitrap analyzer with an automatic gain control (AGC) target of 300%, and a maximum injection time of 50 msec. The most intense ions from the full scan were isolated with an isolation width of 1.6 m/z and fragmented using higher-energy collisional dissociation with a normalized collision energy of 33%. MS/MS spectra were collected in the Orbitrap analyzer (15,000 resolution) with an AGC target of 75% and a maximum injection time of 22 msec.

The resulting MS/MS data were processed using Proteome Discoverer version 2.4 (Thermo Fisher Scientific, Inc.). Tandem mass spectra were searched against the UniProt human protein database (https://www.uniprot.org /taxonomy/9606). Trypsin/P was specified as a cleavage enzyme allowing up to two missing cleavages. The precursor mass tolerance was ±15 ppm, and fragment mass tolerance was ±0.02 Da. Carbamidomethyl on cysteine was defined as a fixed modification, and acetylation at the protein N-terminus and oxidation on methionine were specified as variable modifications. The peptide ion score threshold was set to >20 and high confidence in peptides was required. Search outcomes underwent filtering via a linear discriminant algorithm to achieve an estimated false discovery rate of 1%. Candidate proteins were selected based on the following criteria: i) Intensity ratio (compound/control) ≥2.0, ii) a molecular weight of ~70 kDa (matching the excised band) and iii) protein score ≥10.

*Molecular docking*. The protein structure of ACSL4 was initially predicted using AlphaFold3 (https://github.com/deepmind/alphafold) and was then processed with AutoDockTools 1.5.6 (34) to preserve its original charges and generate a pdbqt file for docking. The 2D structure of Sch B was downloaded from the PubChem database (https://pubchem.ncbi.nlm.nih.gov/compound/108130). Structural optimization was performed using the MOPAC program (https://openmopac.net/) and PM3 atomic charges were calculated. The structure of Sch B was also prepared using AutoDock Tools 1.5.6 to create a pdbqt file. Docking simulations were carried out using AutoDock 4.2.6 (34). A grid box of 100x100x100 points was defined with the center at x=71.637, y=70.446, z=104.536. The grid spacing was 0.375 Å and the exhaustiveness was set to 50. Other docking parameters were set to default and are therefore not listed.

*RNA sequencing*. PANC-1 cells were seeded in 150-mm dishes at a density of $6x10^5$ cells/dish. The cells were then treated with Sch B (20 $\mu$M) or vehicle control (<0.1% DMSO) for 24 h at 37˚C. Total RNA was extracted using RNeasy plus Mini Kit (cat. no. 74134; Qiagen, Inc.) according to the manufacturer's protocol. RNA quality and RNA integrity number (>8.0) were determined using an Agilent 2100 Bioanalyzer (Agilent Technologies, Inc.) with the Agilent RNA 6000 Nano Kit (cat. no. 5067-1511; Agilent Technologies, Inc.). RNA-seq libraries were constructed using the NEBNext® Ultra™ RNA Library Prep Kit (cat. no. E7770; New England BioLabs, Inc.). The libraries were then sequenced on an Illumina NovaSeq 6000 System platform (Illumina, Inc.) with 150 bp paired-end reads. Prior to sequencing, the RNA concentration of the library was determined using a Qubit®2.0 fluorometer (Thermo Fisher Scientific, Inc.) with a Qubit RNA Assay Kit (cat. no. Q32852; Thermo Fisher Scientific, Inc.) and was then diluted to 4 nM. Insert size was assessed using the Agilent Bioanalyzer 2100 system, and qualified insert size was accurately quantified using StepOnePlus™ Real-Time PCR System (Thermo Fisher Scientific, Inc.; library valid concentration >10 nM). mRNA libraries were sequenced on the Illumina sequencing platform by Guangzhou Promegene Biotechnology Co., Ltd.

For data analysis, differential expression analysis was performed using DESeq2 package v1.20.0 (https://bioconductor.org/packages/DESeq2) and the heatmap was generated using the cluster package v2.0.3 (https://cran.r-project.org/web/packages/cluster/) in R v3.6.2 (https://www.r-project.org/). Kyoto Encyclopedia of Genes and Genomes (KEGG) enrichment analysis was performed using the R software clusterProfiler package v3.12.0 (https://bioconductor.org/packages/release/bioc/html/clusterProfiler.html). The raw sequencing data have been deposited into a publicly available database.

*Western blotting (WB)*. MIA PaCa-2 and PANC-1 cells were seeded in 150-mm dishes at a density of $6x10^5$ cells/dish and incubated overnight. The cells were then treated with Sch B (5, 10 or 20 $\mu$M) or vehicle control (<0.1% DMSO) for 24 h at 37˚C. For inhibitor experiments, the cells were pre-treated with Fer-1 (10 $\mu$M) for 4 h followed by treatment with Sch B (20 $\mu$M) for 24 h at 37˚C. Total cellular protein was extracted using RIPA lysis buffer (cat. no. R0010; Beijing Solarbio Science & Technology Co., Ltd.) on ice for 30 min and quantified with a BCA assay kit (cat. no. PC0020; Beijing Solarbio Science & Technology Co., Ltd.). The lysates (30 $\mu$g) were then separated by SDS-PAGE on 4-15% gels, followed by transfer of proteins to PVDF membranes. After blocking with 5% non-fat milk for 1 h at room temperature, the membranes were incubated with the following primary antibodies overnight at 4˚C: Anti-ACSL4 (1:5,000), anti-GSS (1:5,000), anti-SLC3A2 (1:5,000), anti-TF (1:1,000), anti-α-tubulin (1:20,000), anti-GPX4 (1:1,000), anti-SLC7A11 (1:1,000) and anti-GCLC (1:1,000). The membranes were then washed three times with Tris-buffered saline containing 0.1% Tween-20 and were subsequently incubated with HRP-conjugated secondary antibodies (1:10,000; cat. nos. 31430 and 31460; Thermo Fisher Scientific, Inc.) for 2 h at room temperature. Protein bands were visualized using an ECL reagent (cat. no. P1010-500; Applygen Technologies, Inc.). Protein band intensities were semi-quantified using ImageJ version 1.4.3 software and normalized to the corresponding α-tubulin loading control.

*Cell transfection*. MIA PaCa-2 and PANC-1 cells were seeded in 6-well plates at a density $2x10^6$ cells/well and incubated overnight. When the cells reached 50-60% confluence, small interfering (si) RNAs (150 pmol) were transiently introduced into the cells for 6 h at 37˚C using Lipofectamine® RNAiMAX reagent (cat. no. 13778150; Invitrogen; Thermo Fisher Scientific,

Inc.) according to the manufacturer's protocol. A total of 48 h post-transfection, the cells were harvested for WB to verify ACSL4 knockdown efficiency. Cell viability assay, EdU assay, LDH assay and lipid peroxidation assay were carried out as functional experiments. The target and negative control siRNAs were procured from Shanghai GenePharma Co., Ltd. The sequences were as follows: ACSL4 siRNA, 5'-GGG UUGAUAUCUGCAAUAATT-3' (sense), 5'-UUAUUGCAG AUAUCAACCCTT-3' (antisense). Negative control siRNA, 5'-UUCUCCGAACGUGUCACGUTT-3' (sense), 5'-ACGUGA CACGUUCGGAGAATT-3' (antisense).

*Experiments in a xenograft mouse model*. Male Balb/c-nude mice (age, 4-5 weeks; weight, 18.5-22.8 g) were purchased from GemPharmatech Co., Ltd. All mice were housed under specific pathogen-free conditions at the Laboratory Animal Center of Qingyuan People's Hospital, The Sixth Affiliated Hospital of Guangzhou Medical University (Qingyuan, China). The housing conditions were as follows: Temperature, 20-26˚C; humidity, 40-70%; 12-h light/dark cycle; standard rodent chow diet and autoclaved water provided *ad libitum*. Before the experiment, the mice were acclimated for 1 week. All animal procedures were ethically reviewed and approved by the Ethics Committee on Laboratory Animal Care of The Affiliated Qingyuan Hospital (Qingyuan People's Hospital) of Guangzhou Medical University (approval no. LAEC-2023-027). The study was performed in strict compliance with the UK Animals (Scientific Procedures) Act 1986 (https://www.legislation.gov.uk/ukpga/1986/14/contents) and its associated guidelines. PANC-1 cells ($5x10^6$ cells in 100 $\mu$l saline) were injected subcutaneously into the right flank of the mice. Mice were monitored by visual observation and palpation until tumors were detected. On day 10 post-injection, the mice were randomly divided into three treatment groups (n=5 mice/group): Model group (20% SBE-β-CD), a low-dose Sch B group (50 mg/kg) and a high-dose Sch B group (100 mg/kg). Mice received daily oral gavage of Sch B or vehicle for 6 weeks. The body weight and tumor volume were recorded weekly. Tumor volume was calculated using the formula: V=1/2 x (longest axis) x $(\text{shortest axis})^2$.

At the end of the study, mice were euthanized by $CO_2$ exposure at an air displacement rate of 30%/min following anesthesia with isoflurane (2.5% for induction and 1.5% for maintenance in oxygen) to ensure humane conditions. Death was confirmed by cessation of heartbeat and respiration, absence of reflexes and limb paralysis. Humane endpoint criteria followed the Laboratory Animal Guidelines for euthanasia in China (GB/T 39760-2021; https://std.samr.gov.cn/gb/search/gbDetailed?id=BD89DE8E080A3D08E05397BE0A0A4FAD), including a maximum tumor diameter exceeding 15 mm or tumor volume exceeding 1,500 $mm^3$, weight loss exceeding 20% of initial body weight, and an inability to access food or water, as well as difficulties in movement or respiration. No animals required euthanasia or died before the end of the study.

*LSL-Kras$^{G12D/+}$; Trp53$^{flox/+}$; Pdx1-Cre (KPC) mouse model*. LSL-Kras$^{G12D/+}$ (3 male mice; age, 8 weeks; weight, 24.3-26.7 g), Pdx1-Cre (3 male mice; age, 10 weeks; weight, 24.6-25.8 g) and Tp53$^{flox/flox}$ (2 male mice and 2 female mice; age 6 weeks; weight, 21.6-24.5 g) strains on a C57BL/6J background were obtained from Shanghai Model Organisms Center, Inc. The housing conditions were as follows: Temperature, 20-26˚C; humidity, 40-70%; 12-h light/dark cycle; standard rodent chow diet and autoclaved water provided *ad libitum*. Before the experiment, the mice were acclimated for 1 week. To generate KPC mice, LSL-Kras$^{G12D/+}$ mice were first crossed with Trp53$^{flox/flox}$ mice to generate LSL-Kras$^{G12D/+}$; Trp53$^{flox/+}$ offspring. These offspring were then crossed with Pdx1-Cre mice to generate KPC mice, which were genotyped by PCR. At weaning (21-28 days old), KPC mice were anesthetized with isoflurane (2.5% for induction and 1.5% for maintenance in oxygen). A 1-2 mm segment of the tail tip was excised using sterile scissors, after which, the incision was pressed against a sterile gauze pad to achieve hemostasis. For post-operative analgesia, buprenorphine hydrochloride (0.05 mg/kg, subcutaneous) was administered immediately after the procedure, and the mice were placed on a heating pad for recovery. Genomic DNA was extracted from mouse tail samples using a rapid DNA isolation kit (cat. no. NE0400; Leagene; Beijing Regen Biotechnology Co., Ltd.) according to the manufacturer's protocol. PCR was performed in a 20-$\mu$l reaction mixture containing 10 $\mu$l 2X Taq Master Mix (cat. no. P112-02; Vazyme, Inc.), 0.5 $\mu$l each primer (10 $\mu$M), 7 $\mu$l $ddH_2O$ and 2 $\mu$l DNA template. The thermal cycling conditions comprised an initial denaturation step at 94˚C for 3 min; 35 cycles of denaturation at 94˚C for 30 sec, annealing at 58˚C for 30 sec and extension at 72˚C for 30 sec; followed by a final extension at 72˚C for 5 min. The PCR products were electrophoresed on a 1.5% agarose gel (cat. no. BY-R0100; Biowest, Inc.) with Goldview nucleic acid stain (cat. no. AG11915; Hunan Accurate Bio-Medical Technology Co., Ltd.) and visualized under UV light. The primer sequences are listed in Table SI. All animal procedures were ethically reviewed and approved by the Ethics Committee on Laboratory Animal Care of The Affiliated Qingyuan Hospital (Qingyuan People's Hospital) of Guangzhou Medical University (approval no. LAEC-2021-024). The study was performed in strict accordance with the UK Animals (Scientific Procedures) Act 1986 and its associated guidelines. KPC mice (age, 10 weeks; weight, 20.0-27.8 g; 6 male mice and 4 female mice) were randomly divided into two treatment groups (n=5 mice/group): A model group (20% SBE-β-CD) and a Sch B group (100 mg/kg). Mice received daily oral gavage of Sch B or vehicle for 8 weeks and body weight was monitored weekly. Tumor volume was calculated using the formula: V=1/2 x (longest axis) x $(\text{shortest axis})^2$.

At the end of the study, mice were euthanized by $CO_2$ exposure at an air displacement rate of 30%/min following anesthesia with isoflurane (2.5% for induction and 1.5% for maintenance in oxygen) to ensure humane conditions. Death was confirmed by cessation of heartbeat and respiration, absence of reflexes and limb paralysis. Humane endpoint criteria included the emergence of hemorrhagic abdominal ascites, severe cachexia, weight loss exceeding 20% of initial body weight, and inability to access food or water, as well as difficulties in movement or respiration. Mice were observed daily for signs of inactivity and the presence of abdominal ascites. Before the end of study, two KPC mice in the model group developed hemorrhagic abdominal ascites and were euthanized based on the veterinarian's recommendation.

*Biochemical analysis*. At the end of the study, ~200 $\mu$l blood samples were immediately collected from Balb/c-nude mice via cardiac puncture following $CO_2$-induced euthanasia. After clotting at room temperature for 30 min, serum was obtained by centrifuging the blood at 1,000 x g for 10 min at 4˚C and was stored at -80 until further use. Serum samples were used for biochemical analysis. Six biochemical indices, including alanine aminotransferase (ALT), aspartate aminotransferase (AST), creatine kinase (CK), LDH, creatinine (CREA) and uric acid (UA) (cat. nos. 105-020579, 105-020580, 105-020585, 105-00004A, 105-020587 and 105-00023A; Shenzhen Mindray Bio-Medical Electronics Co., Ltd.), were determined according to the manufacturer's protocol using an automatic biochemical analyzer (Shenzhen Mindray Bio-Medical Electronics Co., Ltd.) to evaluate the effects of Sch B on liver, heart and kidney function.

*Histological analysis and immunohistochemistry*. Tumor tissues and major organs were fixed in 4% paraformaldehyde for 24 h at room temperature, embedded in paraffin and sectioned into 3-$\mu$m slices. Following deparaffinization and rehydration, the sections were stained with hematoxylin for 10 min and eosin for 10 sec at room temperature, then dehydrated and mounted for examination. For immunohistochemistry, the paraffin-embedded sections were deparaffinized and rehydrated, followed by immersion in citrate buffer (pH 6.0) at 100˚C for 2.5 min for antigen retrieval. Endogenous peroxidase activity was blocked with 3% hydrogen peroxide for 30 min at room temperature. The sections were then permeabilized with 0.5% Triton X-100 solution for 10 min and blocked with 10% normal goat serum (cat. no. SL038; Beijing Solarbio Science & Technology Co., Ltd.) for 30 min at room temperature. Subsequently, the sections were incubated with primary antibodies against ACSL4 (1:500) and Ki67 (1:200; cat. no. ab16667; Abcam) overnight at 4˚C. After rinsing, the sections were incubated with an undiluted HRP-conjugated secondary antibody (cat. no. PR30009, Proteintech Group, Inc.) for 2 h at room temperature. The reaction was visualized using DAB (cat. no. PK001; Abcarta, Inc.) for 0.5-1 min followed by counterstaining with hematoxylin for 5 min at room temperature. Finally, the sections were sealed using an automatic sealing machine (Tissue-Tek® Film; Sakura Finetek Japan Co., Ltd.), and images were captured using a light microscope (Olympus Corporation) and semi-quantitatively analyzed with ImageJ version 1.4.3 software.

*Statistical analysis*. All data are presented as mean ± standard error of the mean. All *in vitro* experiments were performed three times and representative experiments are shown. Comparisons between two groups were performed by unpaired Student's t-test. Multiple comparisons were analyzed using one-way analysis of variance followed by Dunnett's post hoc test. Data were analyzed using GraphPad Prism 8 (Dotmatics). $P<0.05$ was considered to indicate a statistically significant difference.

## Results

*Sch B inhibited the proliferation of PC cells and induces cell death*. The chemical structure of Sch B is illustrated in Fig. 1A. PC cell lines (MIA PaCa-2, PANC-1 and PL45) and a normal pancreatic epithelial cell line (hTERT-HPNE) were treated with varying concentrations of Sch B for the indicated times, and cell proliferation was assessed by CCK-8, colony formation, and EdU assays. The CCK-8 results showed that Sch B significantly inhibited the viability of all PC cell lines in a concentration- and time-dependent manner; the half maximal inhibitory concentration values at 24 h were 11.8 $\mu$M for MIA PaCa-2 cells, 11.5 $\mu$M for PANC-1 cells and 15.27 $\mu$M for PL45 cells (Fig. 1B). Notably, hTERT-HPNE cells were substantially less sensitive than the cancer cells. Because MIA PaCa-2 and PANC-1 exhibited greater sensitivity to Sch B, they were selected for all subsequent mechanistic and functional experiments. Colony formation assays (Fig. 1C) and EdU staining (Fig. 1D) confirmed these findings. To determine whether Sch B induces cell death, LDH release and Trypan blue staining assays were performed. The LDH assay indicated that Sch B significantly increased the cell death rate in a concentration-dependent manner (Fig. 1E). Similar results were obtained from the Trypan blue staining assay (Fig. 1F). Together, these findings indicated that Sch B may effectively inhibit PC cell proliferation and induce cell death.

*Cell death induced by Sch B is associated with ferroptosis*. To investigate the mechanisms underlying Sch B-induced cell death in PC cells, RNA sequencing was performed on PANC-1 cells treated with 20 $\mu$M Sch B. A total of 4,101 significant differentially expressed genes (DEGs) were identified between the Sch B group and the control group; among them, 2,525 DEGs were upregulated and 1,576 DEGs were downregulated (Fig. 2A and B). KEGG pathway enrichment analysis revealed that the upregulated DEGs were most significantly enriched in the 'ferroptosis' pathway (Fig. 2C). Downregulated DEGs were predominantly enriched in 'Oxidative phosphorylation', 'Chemical carcinogenesis-reactive oxygen species', 'Alanine, aspartate and glutamate metabolism', and 'Glutathione metabolism' pathways; these pathways are closely associated with ferroptosis (Fig. 2D). To further investigate the mode of cell death induced by Sch B, specific inhibitors of cell death were utilized in MIA PaCa-2 and PANC-1 cells. As shown in Fig. 2E and F, the ferroptosis inhibitors Fer-1 and DFO, the apoptosis inhibitor Z-VAD-FMK and the ROS scavenger NAC effectively reversed the inhibitory effects of Sch B on cell viability. By contrast, the necroptosis inhibitor NEC-1 did not affect Sch B-induced cell viability. These findings indicated that ferroptosis may be partially involved in Sch B-induced PC cell death.

*Sch B triggers ferroptosis in PC cells*. Intracellular iron overload and lipid peroxidation of membranes are hallmark features of ferroptosis. The results of FerroOrange staining and the C11-BODIPY assay showed that Sch B dose-dependently increased the levels of $Fe^{2+}$ (Fig. 3A) and lipid peroxidation (Fig. 3B) in both MIA PaCa-2 and PANC-1 cells. Sch B also significantly elevated MDA, a marker of lipid peroxidation, while concurrently reducing GSH levels (Fig. 3D). Morphologically, ferroptotic cells exhibit distinct ultrastructural changes in the mitochondria; therefore, subcellular changes in Sch B-treated cells were observed. Transmission electron microscopy revealed that mitochondria in the Sch B group appeared rounder and smaller, with denser membranes

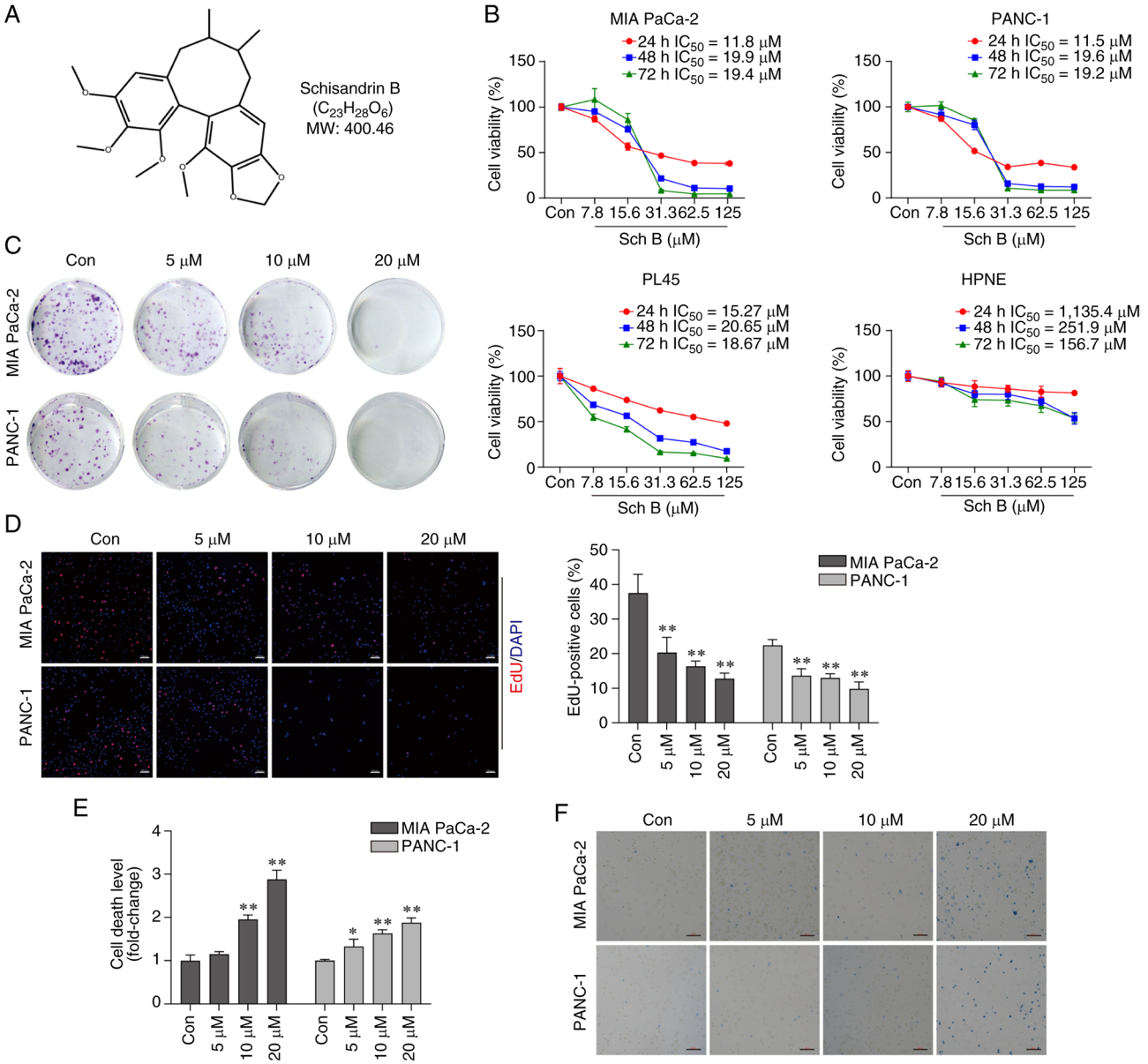


Figure 1. Sch B inhibits the proliferation of pancreatic cancer cells and induces cell death *in vitro*. (A) Chemical structure of Sch B. (B) Viability of MIA PaCa-2, PANC-1, PL45 and hTERT-HPNE cells was assessed using Cell Counting Kit-8 assay. Cell proliferation in MIA PaCa-2 and PANC-1 cells was evaluated using (C) colony formation assay and (D) EdU staining. Scale bars, 50 $\mu$m. Cell death in MIA PaCa-2 and PANC-1 cells was measured using (E) lactate dehydrogenase cytotoxicity assay and (F) Trypan blue staining. Scale bars, 500 $\mu$m. $^{*}$P<0.05, $^{**}$P<0.01 vs. Con. Con, control; $IC_{50}$, half maximal inhibitory concentration; MW, molecular weight; Sch B, Schisandrin B.

and fewer cristae, which is a typical feature of ferroptosis (Fig. 3C). Subsequently, the expression levels of proteins involved in iron metabolism, GSH metabolism and lipid peroxidation were assessed. The results showed that Sch B upregulated the expression levels of ACSL4 and SLC3A2, and downregulated GPX4, GCLC and GSS, whereas TF and SLC7A11 exhibited no notable changes in PC cells (Fig. 3E). Collectively, these findings indicated that Sch B may induce ferroptosis in PC cells, at least in part by increasing iron availability and promoting lipid peroxidation, while suppressing glutathione synthesis and antioxidant defenses.

*Blocking ferroptosis reverses Sch B-induced cell death*. To elucidate the involvement of ferroptosis in the antitumor effects of Sch B, the ferroptosis inhibitor Fer-1 was used *in vitro*. Fer-1 pre-treatment effectively prevented Sch B-induced cell death (Fig. 4A) and significantly diminished the inhibitory effect of Sch B on cell proliferation (Fig. 4B). Moreover, Fer-1 pre-treatment significantly decreased Sch B-induced $Fe^{2+}$ levels (Fig. 4C), lipid peroxidation (Fig. 4D), and MDA levels (Fig. 4E), whereas it significantly increased GSH levels (Fig. 4E). WB revealed that Fer-1 pre-treatment also reversed the Sch B-induced upregulation of ACSL4 and downregulation of GPX4 (Fig. 4F). Collectively, these findings suggested that ferroptosis may be the predominant mechanism underlying Sch B-induced PC cell death.

*Sch B promotes ACSL4-mediated ferroptosis in PC cells*. To explore the molecular mechanism of Sch B-induced ferroptosis, DARTS and mass spectrometry analyses conducted

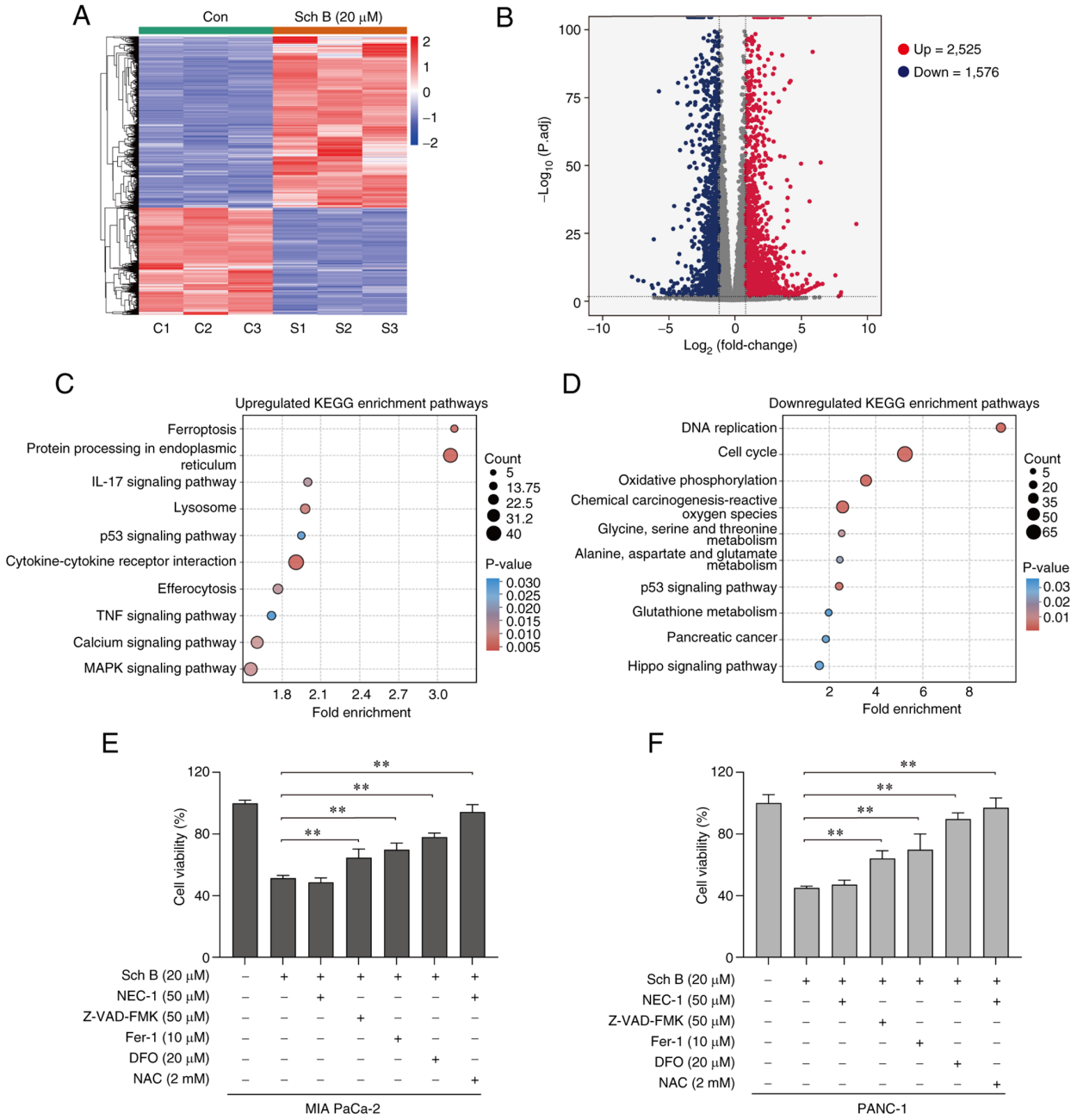


Figure 2. Cell death induced by Sch B is associated with ferroptosis. (A) Heat map and (B) volcano plot of the DEGs in PANC-1 cells between the Sch B group and the control group. KEGG annotation and enrichment analysis of the (C) upregulated and (D) downregulated DEGs in PANC-1 cells. Viability of (E) MIA PaCa-2 and (F) PANC-1 cells treated with Sch B (20 $\mu$M) with or without inhibitors, NEC-1 (50 $\mu$M), Z-VAD-FMK (50 $\mu$M), Fer-1 (10 $\mu$M), DFO (20 $\mu$M) and NAC (2 mM), was assessed using Cell Counting Kit-8 assay. $^{**}$P<0.01. Con, control; DEG, differentially expressed gene; DFO, deferoxamine mesylate; Fer-1, ferrostatin-1; KEGG, Kyoto Encyclopedia of Genes and Genomes; NAC, N-acetylcysteine; NEC-1, necrostatin-1; Sch B, Schisandrin B.

in PANC-1 cells were. The results showed that a protein band with a molecular weight of ~70 kDa was distinctly protected by Sch B (Fig. 5A). Mass spectrometry identified 136 proteins as potential targets with significant differences (intensity ratio ≥2.0). KEGG pathway enrichment analysis revealed that the potential target proteins were enriched in the 'ferroptosis' pathway. Based on the combination of intensity ratio ≥2.0, molecular weight matching the protected band (~70 kDa), and protein score ≥10.0, ACSL4 was identified as a promising candidate (Fig. 5B). Molecular docking was performed between Sch B and the predicted protein structure of ACSL4; the binding energy was-6.043 kcal/mol, indicating a potential interaction (Fig. 5C). Based on these results, it was hypothesized that Sch B may promote ferroptosis by interacting with ACSL4. To test this hypothesis, ACSL4 was silenced using siRNA in PANC-1 cells before Sch B treatment (Fig. 5D). ACSL4 knockdown effectively reduced the sensitivity of PC cells to Sch B, as evidenced by restored cell viability (Fig. 5E) and proliferative capacity (Fig. 5F). Additionally, ACSL4 knockdown protected against Sch B-induced cell death (Fig. 5G) and reduced lipid peroxidation (Fig. 5H). These findings confirmed that Sch B induces ferroptosis by activating the ACSL4-regulated ferroptosis pathway in PC cells.

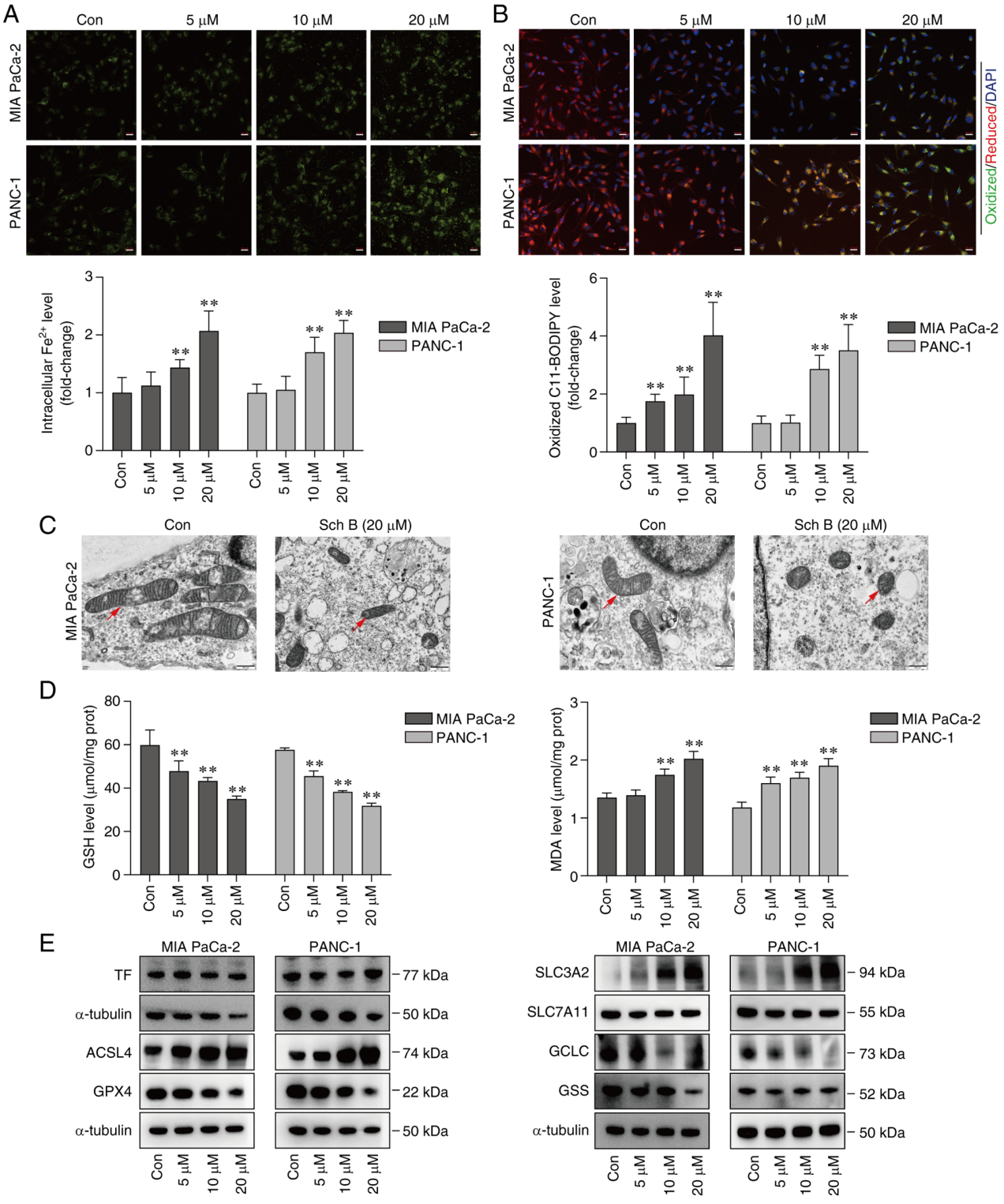


Figure 3. Sch B triggers ferroptosis in pancreatic cancer cells. (A) Intracellular $Fe^{2+}$ levels in MIA PaCa-2 and PANC-1 cells were detected by FerroOrange probe. Scale bars, 20 $\mu$m. (B) Lipid peroxidation levels of MIA PaCa-2 and PANC-1 were detected by C11-BODIPY 581/591 fluorescent probe. Scale bars, 20 $\mu$m. (C) Transmission electron microscopy imaging of mitochondrial ultrastructure in MIA PaCa-2 and PANC-1 cells was conducted. Scale bars, 500 nm. Red arrowheads indicate mitochondria. (D) Levels of GSH and MDA in MIA PaCa-2 and PANC-1 cells were measured using ELISA kits. (E) Expression levels of ferroptosis-related proteins in MIA PaCa-2 and PANC-1 cells were detected by western blotting. $^{**}$P<0.01 vs. Con. ACSL4, acyl-CoA synthetase long-chain family member 4; Con, control; GCLC, γ-glutamyl-cysteine ligase catalytic subunit; GPX4, glutathione peroxidase 4; GSH, glutathione; GSS, glutathione synthetase; MDA, malondialdehyde; Sch B, Schisandrin B; SLC3A2, solute carrier family 3 member 2; SLC7A11, solute carrier family 7 member 11; TF, transferrin.

*Sch B exerts antitumor efficacy by inducing ferroptosis in vivo*. To assess the therapeutic efficacy of Sch B *in vivo*, two murine models were established: A subcutaneous xenograft tumor model and a genetically engineered orthotopic spontaneous pancreatic tumor model (KPC). In the xenograft model, Sch B treatment led to a significant dose-dependent

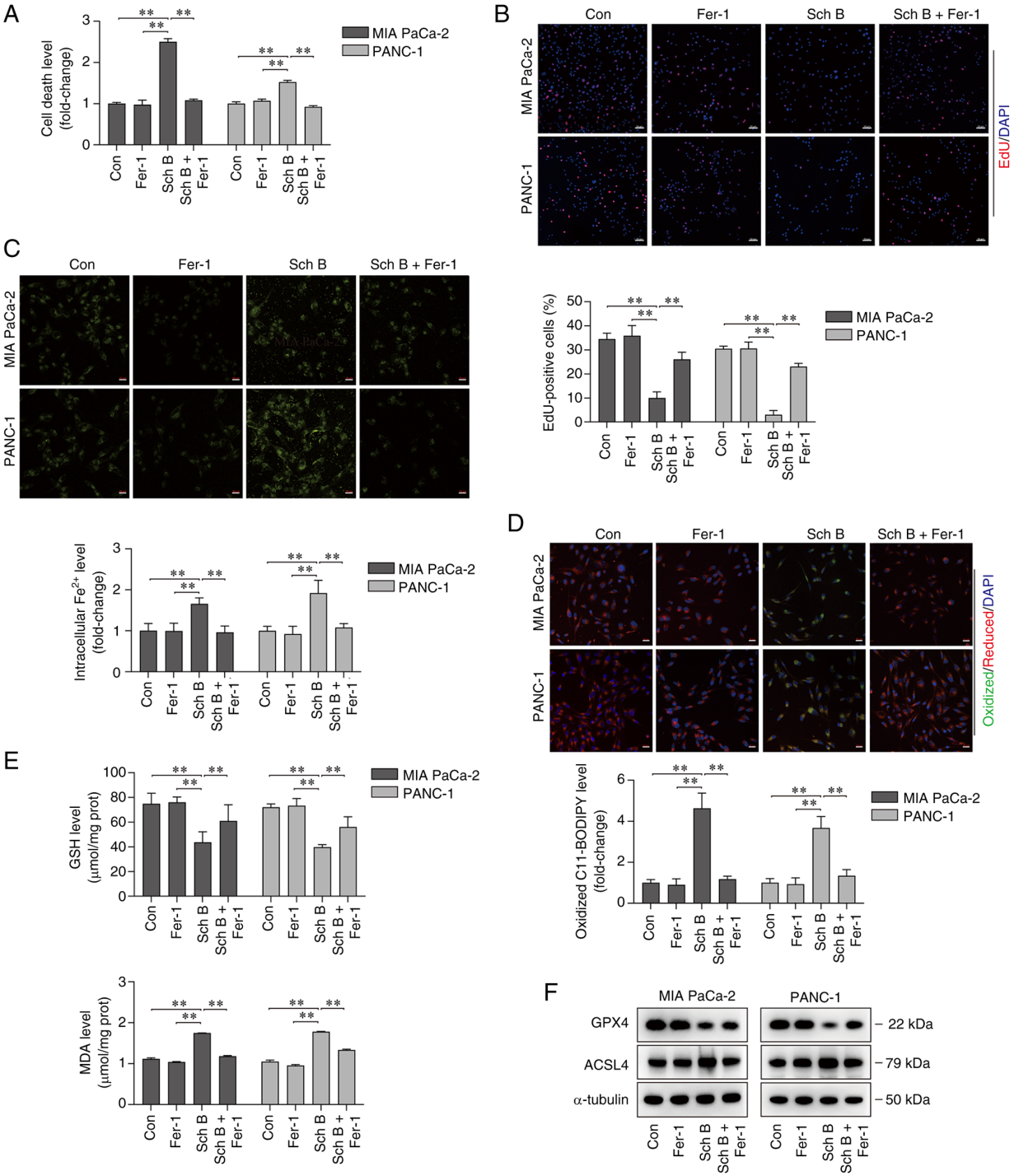


Figure 4. Fer-1 blocks Sch B-mediated ferroptosis in pancreatic cancer cells. (A) Cell death of MIA PaCa-2 and PANC-1 cells treated with Sch B (20 $\mu$M) with or without Fer-1 (10 $\mu$M) was measured using lactate dehydrogenase cytotoxicity assay. (B) Cell proliferation of MIA PaCa-2 and PANC-1 cells treated with Sch B (20 $\mu$M) with or without Fer-1 (10 $\mu$M) was evaluated using EdU staining. Scale bars, 50 $\mu$m. (C) Intracellular $Fe^{2+}$ levels of MIA PaCa-2 and PANC-1 cells treated with Sch B (20 $\mu$M) with or without Fer-1 (10 $\mu$M) were detected using FerroOrange probe. Scale bars, 20 $\mu$m. (D) Lipid peroxidation levels of MIA PaCa-2 and PANC-1 cells treated with Sch B (20 $\mu$M) with or without Fer-1 (10 $\mu$M) were detected using C11-BODIPY 581/591 fluorescent probe. Scale bars, 20 $\mu$m. (E) GSH and MDA levels of MIA PaCa-2 and PANC-1 cells treated with Sch B (20 $\mu$M) with or without Fer-1 (10 $\mu$M) were measured using kits. (F) Protein expression levels of ACSL4 and GPX4 in MIA PaCa-2 and PANC-1 cells treated with Sch B (20 $\mu$M) with or without Fer-1 (10 $\mu$M) were detected by western blotting. $^{**}$P<0.01. ACSL4, acyl-CoA synthetase long-chain family member 4; Con, control; Fer-1, ferrostatin-1; GPX4, glutathione peroxidase 4; GSH, glutathione; MDA, malondialdehyde; Sch B, Schisandrin B.

inhibition of tumor growth; this was evidenced by reduced tumor weight and volume compared with in the model group (Fig. 6A and B). Immunohistochemical analysis showed a decrease in Ki67-positive cells and an increase in ACSL4 expression after Sch B treatment (Fig. 6C). Furthermore, the role of Sch B in cancer development and metastasis was investigated using the KPC model. Starting at 10 weeks of age, KPC mice received daily oral administration of Sch B (100 mg/kg) or vehicle. Gross pathological examination revealed a substantial pancreatic tumor burden occupying

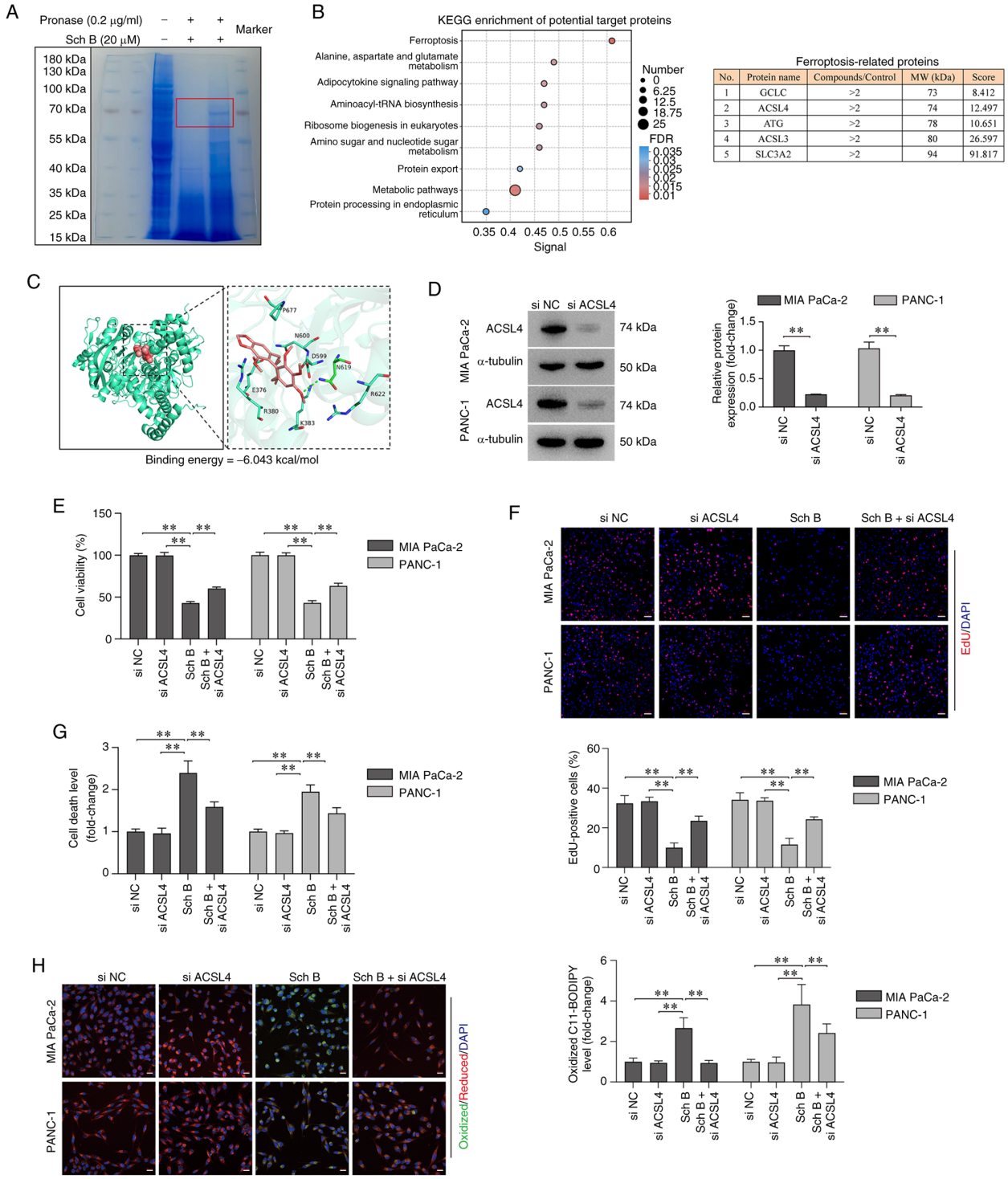


Figure 5. Sch B induces ACSL4-dependent ferroptosis in pancreatic cancer cells. (A) Coomassie blue staining of drug affinity responsive target stability assay. A band with a molecular weight of ~70 kDa was protected by Sch B. (B) KEGG enrichment analysis of potential target proteins identified by mass spectrometry. (C) Molecular docking analysis of the interactions between Sch B and ACSL4. (D) Interference efficiency of si ACSL4 in MIA PaCa-2 and PANC-1 cells. (E) Cell viability was assessed using Cell Counting Kit-8 assays in MIA PaCa-2 and PANC-1 cells. (F) EdU staining was used to detect the proliferation of MIA PaCa-2 and PANC-1 cells. Scale bars, 50 $\mu$m. (G) Lactate dehydrogenase cytotoxicity assay was used to determine the cell death of MIA PaCa-2 and PANC-1 cells. (H) Lipid peroxidation levels were detected using C11-BODIPY 581/591 fluorescent probe in MIA PaCa-2 and PANC-1 cells. Scale bars, 20 $\mu$m. $^{**}$P<0.01. ACSL4, acyl-CoA synthetase long-chain family member 4; Con, control; KEGG, Kyoto Encyclopedia of Genes and Genomes; MW, molecular weight; NC, negative control; Sch B, Schisandrin B; si, small interfering.

most of the pancreatic space in the model group. By contrast, mice treated with Sch B displayed significantly smaller tumors with preserved pancreatic architecture (Figs. 6D and S1). Histological analysis indicated that mice in the model group developed poorly differentiated tumors characterized by a prominent desmoplastic stroma and complete loss of normal acinar structure. Conversely, Sch B-treated mice exhibited moderately differentiated tumors with decreased stromal density and residual normal pancreatic tissue (Fig. 6E). Immunohistochemical analysis confirmed that Sch B treatment

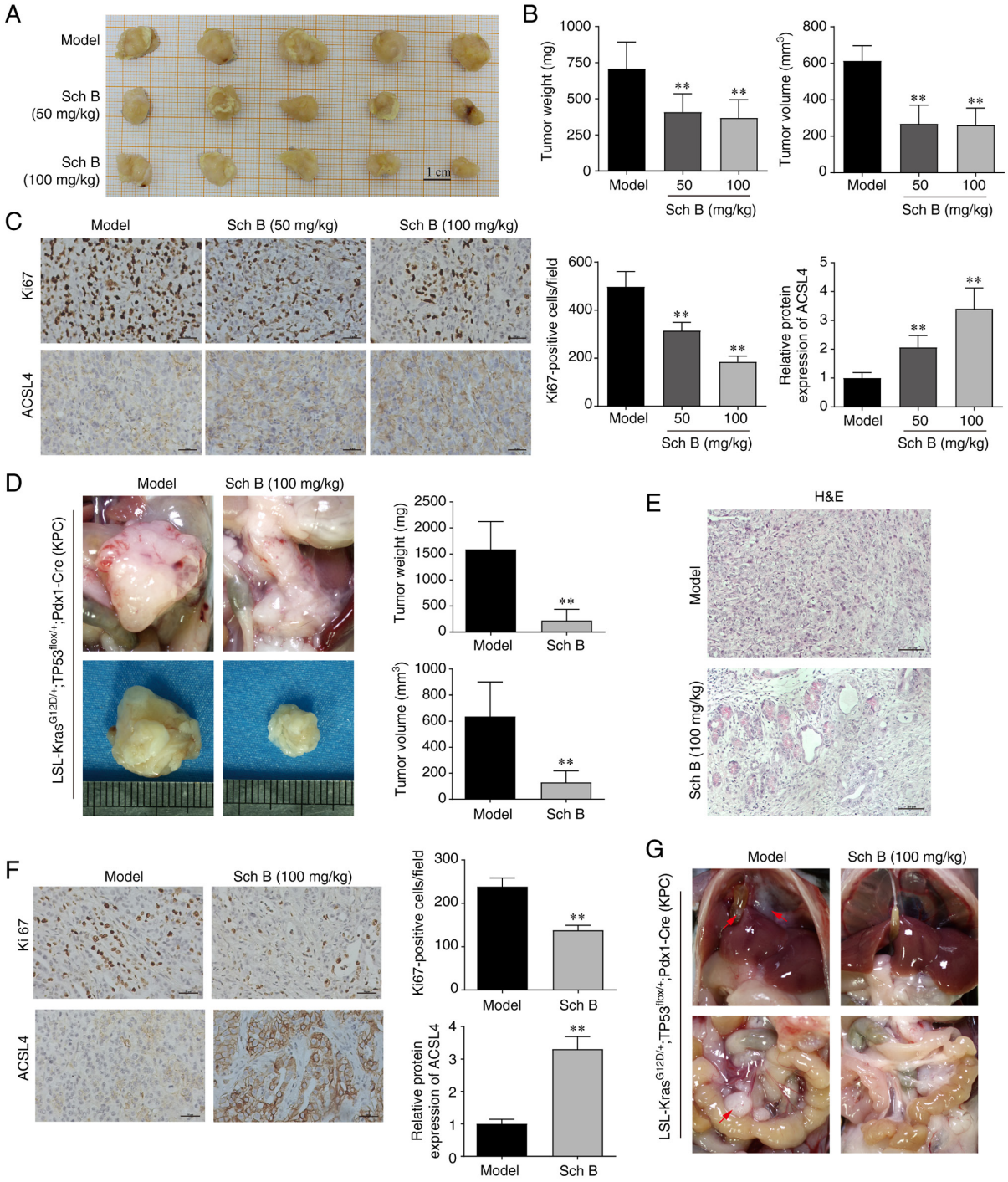


Figure 6. Sch B suppresses tumor progression *in vivo*. (A) Representative images of tumors in PANC-1 xenograft mice. (B) Tumor weight and volume of mice in each group. (C) Immunohistochemistry detected the expression of Ki67 and ACSL4 in tumor tissues. Scale bars, 50 $\mu$m. (D) Representative macroscopic images of tumors in KPC mice. (E) H&E staining showing the degree of tissue differentiation in each group. Scale bars, 100 $\mu$m. (F) Immunohistochemistry detected the expression of Ki67 and ACSL4 in tumor tissues. Scale bars, 50 $\mu$m. (G) Representative images of abdominal metastases observed in KPC mice. Red arrowheads indicate metastatic foci. $^{**}$P<0.01 vs. model. ACSL4, acyl-CoA synthetase long-chain family member 4; H&E, hematoxylin and eosin; KPC, LSL-Kras$^{G12D/+}$; TP53$^{flox/+}$; Pdx1-Cre; Sch B, Schisandrin B.

significantly reduced Ki67-positive cells and increased ACSL4 expression compared with in the model group (Fig. 6F). Notably, all model mice (5/5) developed abdominal metastases (mesenteric: 5/5; liver: 3/5; diaphragmatic: 3/5; bile duct: 2/5; peritoneal: 2/5); by contrast, only one Sch B-treated mice showed metastatic lesions (mesenteric: 1/5) (Fig. 6G). Additionally, toxicological assessments in xenograft mice indicated that Sch B treatment significantly increased relative liver weight, but had no effect on body weight or the relative weights of other organs (Fig. 7A). Histological examination revealed no observable systemic organ toxicity compared with in the model group (Fig. 7B). Serum biochemical analysis revealed no significant differences in ALT, AST, CK, LDH, CREA and UA levels between the Sch B-treated group and the model group (Fig. 7C). Overall, Sch B effectively suppressed tumor growth *in vivo* by promoting ferroptosis.

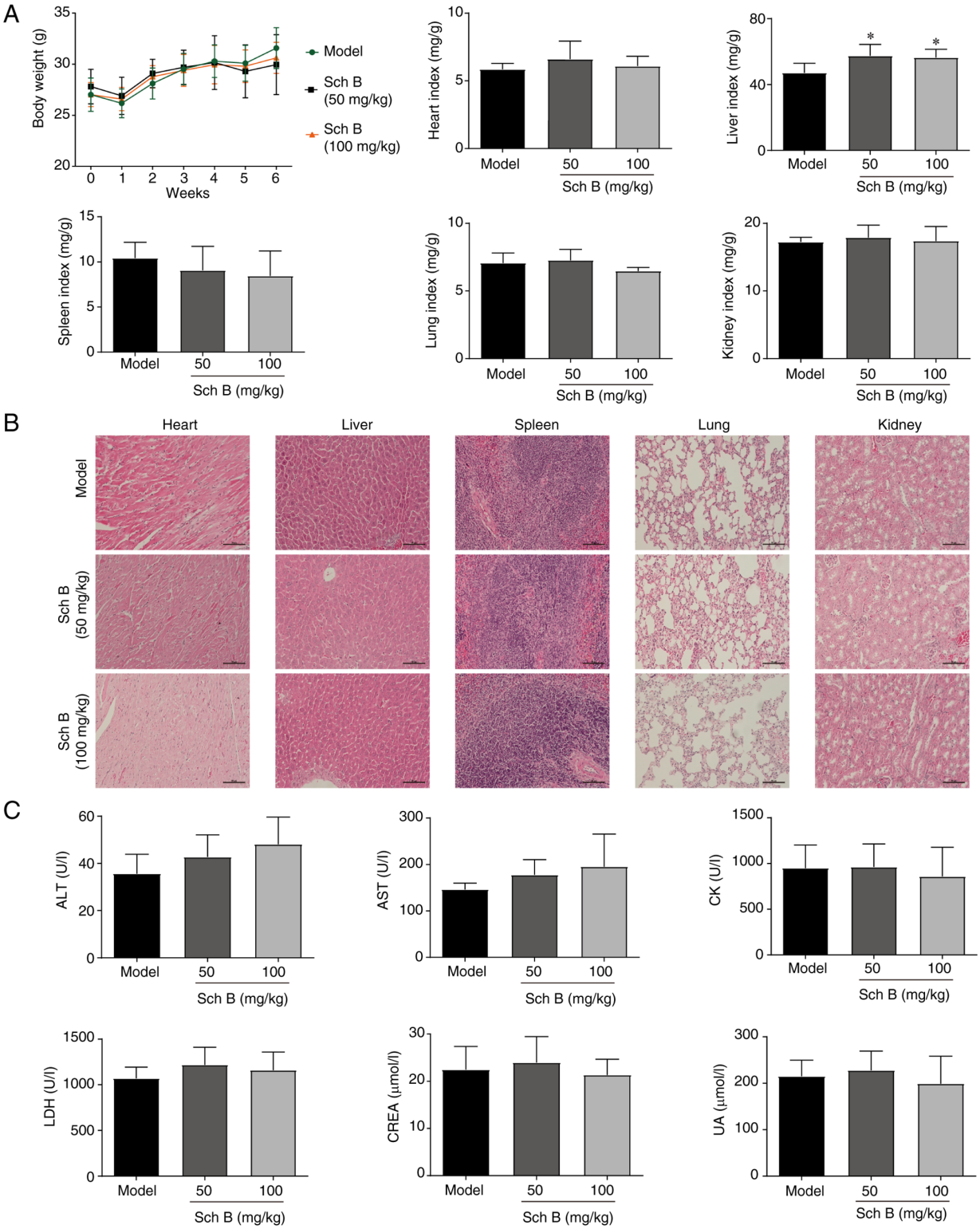


Figure 7. Evaluation of the potential toxicity of Sch B in PANC-1 xenograft mice. (A) Body weight and relative organ weight of mice in each group. (B) Hematoxylin and eosin staining of organs in each group. Scale bars, 100 $\mu$m. (C) Levels of ALT, AST, CK, LDH, CREA and UA in serum. *P<0.05 vs. model. ALT, alanine aminotransferase; AST, aspartate aminotransferase; CK, creatine kinase; CREA, creatinine; LDH, lactate dehydrogenase; Sch B, Schisandrin B; UA, uric acid.

## Discussion

PC is one of the most lethal malignant tumors of the digestive system, with limited treatment options (4). For advanced PC, multiagent chemotherapy regimens provide only modest survival benefits over gemcitabine alone (35). Consequently, more effective treatments are urgently needed. Natural-product-based herbal medicines represent valuable resources for drug discovery in PC due to their established efficacy and safety profiles (36,37). Sch B, the main active

compound derived from *Schisandra chinensis* (Turcz.) Baill., exhibits antitumor activity against various types of human cancer. For example, our recent study revealed that Sch B can inhibit hepatocellular carcinoma progression by disrupting the crosstalk between macrophages and hepatoma cells (38). However, to the best of our knowledge, its therapeutic efficacy in PC has yet to be investigated. The present findings now confirm that Sch B inhibits PC cell proliferation and induces cell death, without exhibiting overt cytotoxic effects on normal pancreatic epithelial cells (HPNE); therefore, Sch B is a promising potential treatment for PC.

Ferroptosis was initially characterized as iron-dependent oxidative cell death occurring in KRAS-mutant tumor cells (39). Oncogenic KRAS mutations are present in >90% of patients with PC, and KRAS-mutant PC cells exhibit heightened susceptibility to ferroptosis, making it a promising therapeutic strategy (40,41). Several natural compounds, including Wogonin, Tiliroside and Solasonine, inhibit PC growth by inducing ferroptosis (42-44). However, whether Sch B induces ferroptosis in PC remained unclear. In the current study, transcriptome analysis of Sch B-treated PANC-1 cells revealed significant enrichment of ferroptosis-related pathways, such as oxidative phosphorylation, ROS, glutamate and glutathione metabolism. Pharmacological experiments using inhibitors indicated that the ferroptosis inhibitor Fer-1 partially rescued Sch B-induced cell death. Furthermore, transmission electron microscopy further demonstrated shrunken mitochondria with increased membrane density and reduced cristae, which are characteristic features of ferroptosis (45). Additionally, Sch B induced iron overload, lipid peroxidation, GSH depletion, MDA accumulation and altered expression of key ferroptosis-related proteins. Notably, these changes were reversed by Fer-1. Based on these results, it may be hypothesized that ferroptosis is partially involved in Sch B-induced cell death in PC.

Lipid peroxidation is the major signal for ferroptosis and is mediated by both enzymatic and non-enzymatic Fenton reaction pathways (46). Polyunsaturated fatty acid (PUFA)-containing phospholipids are the primary substrates for peroxidation in ferroptosis, which is regulated by various catalytic enzymes, including ACSL4, lysophosphatidylcholine acyl-transferase 3 and lipoxygenases. ACSL4 promotes the biosynthesis of lipids with PUFA by catalyzing the esterification of arachidonic acid and adrenic acid with phosphatidylethanolamine, which is a vital initiator of ferroptosis (47). Several studies have highlighted the pro-ferroptotic role of ACSL4 in PC cells. For example, dipeptidyl peptidase-4 stabilizes ACSL4 to enhance ferroptosis sensitivity, and protein tyrosine phosphatase mitochondrial 1 knockdown upregulates ACSL4 to sensitize PC cells to erastin-induced ferroptosis (48,49). Conversely, low ACSL4 expression in PC is associated with poor prognosis, and ACSL4-mediated suppression of ferroptosis contributes to resistance against chemotherapy and immunotherapy in PC cells (50-52). The present study revealed that Sch B significantly upregulated ACSL4 expression in PC cells. Using DARTS and molecular docking analysis, ACSL4 was identified as a target protein for Sch B, and ACSL4 knockdown abolished Sch B-induced ferroptosis. Complementing these *in vitro* findings, Sch B significantly inhibited tumor growth in both xenograft and KPC models, increased ACSL4 expression and reduced metastasis, with no overt toxicity. These results suggested that Sch B inhibits PC through ACSL4-dependent ferroptosis.

The present findings add to the growing body of evidence supporting the potential of targeting metabolic pathways, particularly ferroptosis, for treating aggressive gastrointestinal malignancies, including PC. These data align with the concept that ferroptosis is a targetable vulnerability in cancer characterized by high levels of iron and ROS (53). More broadly, PCD, including pyroptosis, necroptosis, PANoptosis or autophagy, have garnered increasing attention in neoplastic diseases. These PCD pathways can either inhibit tumorigenesis or facilitate tumor progression, immune escape and chemoresistance, depending on the cellular context (54-59). For example, c-MYC upregulation drives resistance to anti-EGFR treatment in metastatic colorectal cancer, exemplifying how oncogenic signaling reprogramming can undermine targeted treatment efficacy (60). The interplay among these different modes of cell death is further complicated by microbial factors. Notably, *Fusobacterium nucleatum* potentiates gastric tumorigenesis by altering the tumor microenvironments and enhancing immune evasion, underscoring the relevance of infectious agents as modulators of cell death (61). These observations reveal the complexity of cell death in gastrointestinal malignancies and suggest that effective ferroptosis-based therapies must consider this broader network, which includes potential interactions with microbial and metabolic factors.

The pharmacokinetic (PK) and pharmacodynamic (PD) profiles of Sch B are important considerations for its clinical translation. Although PK/PD parameters were not assessed in the present study, prior findings have indicated that Sch B is orally bioavailable and tends to accumulate in tumor tissues. A PK study in rats reported an absolute oral bioavailability of ~55.0% at a dose of 10 mg/kg, with linear PK properties observed at 10-40 mg/kg (62). Oral administration of Sch B at 150 mg/kg resulted in peak plasma concentrations ranging between 5.9 and 10.2 $\mu$M in rats, which aligned well with the effective dose identified in *in vitro* assays (63). Additionally, a PD study in mice revealed that Sch B effectively reached and accumulated at high levels in tumor tissues (64). Notably, the orthotopic KPC model presents a substantially greater drug delivery barrier than xenograft models, owing to the dense desmoplastic stroma typical of PC. The potent antitumor efficacy observed in this challenging model, along with existing PK evidence, strongly indicates that pharmacologically relevant concentrations of Sch B can be attained *in vivo*. However, direct measurement of intra-tumoral concentrations, systemic half-life and the maximum tolerated dose of Sch B in this model remains necessary. Future studies should include comprehensive PK/PD characterization of Sch B in plasma and tumor tissue to establish a clear dose-exposure-response relationship.

In conclusion, the present study revealed a novel mechanism by which Sch B inhibits PC at least partially via the ACSL4-dependent ferroptosis pathway. However, the current

study has certain limitations. The direct binding between ACSL4 and Sch B requires further verification, and addressing this issue in future studies will strengthen its potential for clinical application.

**Acknowledgements**

Not applicable.

**Funding**

This work was supported by the Medical Science and Technology Foundation of Guangdong Province (grant no. A2024690), the Scientific Research Project of Guangdong Bureau of Traditional Chinese Medicine (grant no. 20251478), the Wu JiePing Medical Foundation (grant no. 320.6750.2024-03-49), the Guangdong Basic and Applied Basic Research Foundation (grant nos. 2025A1515010072 and 2024A1515220029) and the Research Capability Enhancement Program of Guangzhou Medical University (grant no. GMUCR2024-02003).

**Availability of data and materials**

The proteomics data generated in the present study may be found in the iProX under accession number IPX0017006000/PXD078099 or at the following URL: https://www.iprox.cn//page/project.html?id=IPX0017006000. The raw sequencing data generated in the present study may be found in the Gene Expression Omnibus under accession number GSE315793 or at the following URL: https://www.ncbi.nlm.nih.gov/geo/query/acc.cgi?acc=GSE315793. The other data generated in the present study may be requested from the corresponding author.

**Authors' contributions**

FL, LQ and TP designed the study. FL, JF and XL performed most of the experiments. LY, YLiu and YLi performed some experiments. FL and JF analyzed and interpreted the data. FL, LQ and TP wrote and edited the manuscript. All authors read and approved the final version of the manuscript. FL, JF and LQ confirm the authenticity of all the raw data. All authors read and approved the final manuscript.

**Ethics approval and consent to participate**

All animal procedures were ethically reviewed and approved by the Ethics Committee on Laboratory Animal Care of The Affiliated Qingyuan Hospital (Qingyuan People's Hospital) of Guangzhou Medical University (approval nos. LAEC-2021-024 and LAEC-2023-027).

**Patient consent for publication**

Not applicable.

**Competing interests**

The authors declare that they have no competing interests.

**References**

1. Siegel RL, Miller KD, Wagle NS and Jemal A: Cancer statistics, 2023. CA Cancer J Clin 73: 17-48, 2023.
2. Xia C, Dong X, Li H, Cao M, Sun D, He S, Yang F, Yan X, Zhang S, Li N and Chen W: Cancer statistics in China and United States, 2022: Profiles, trends, and determinants. Chin Med J (Engl) 135: 584-590, 2022.
3. Zeng H, Zheng R, Sun K, Zhou M, Wang S, Li L, Chen R, Han B, Liu M, Zhou J, *et al*: Cancer survival statistics in China 2019-2021: A multicenter, population-based study. J Natl Cancer Cent 4: 203-213, 2024.
4. Park W, Chawla A and O'Reilly EM: Pancreatic cancer: A review. JAMA 326: 851-862, 2021.
5. Strobel O, Neoptolemos J, Jäger D and Büchler MW: Optimizing the outcomes of pancreatic cancer surgery. Nat Rev Clin Oncol 16: 11-26, 2019.
6. Siegel RL, Miller KD, Fuchs HE and Jemal A: Cancer statistics, 2021. CA Cancer J Clin 71: 7-33, 2021.
7. Halbrook CJ, Lyssiotis CA, Pasca di Magliano M and Maitra A: Pancreatic cancer: Advances and challenges. Cell 186: 1729-1754, 2023.
8. Grossberg AJ, Chu LC, Deig CR, Fishman EK, Hwang WL, Maitra A, Marks DL, Mehta A, Nabavizadeh N, Simeone DM, *et al*: Multidisciplinary standards of care and recent progress in pancreatic ductal adenocarcinoma. CA Cancer J Clin 70: 375-403, 2020.
9. Sharma R, Kumar S, Ghosh R, Komal K and Kumar M: Gene therapy: Transforming the battle against pancreatic cancer. Curr Gene Ther 26: 152-159, 2026.
10. Liaki V, Barrambana S, Kostopoulou M, Lechuga CG, Zamorano-Dominguez E, Acosta D, Morales-Cacho L, Álvarez R, Sun P, Rosas-Perez B, *et al*: A targeted combination therapy achieves effective pancreatic cancer regression and prevents tumor resistance. Proc Natl Acad Sci USA 122: e2523039122, 2025.
11. Luo X and Gao Z: MARVELD1 promotes the invasiveness in pancreatic adenocarcinoma through the activation of epithelial-to-mesenchymal transition. Protein Pept Lett 32: 224-233, 2025.
12. Song G, Qi X and Zhao Y: iRGD tumor penetrating peptide-modified NK cells exhibit enhanced tumor immune infiltration ability and anti-tumor efficacy. Protein Pept Lett 32: 183-193, 2025.
13. Kaviyaprabha R, Miji TV, Sreelakshmi PS, Muthusami S, Arulselvan P and Bharathi M: Unveiling the potential role of hesperetin and emodin as a combination therapy to inhibit the pancreatic cancer progression against the C-met gene. Protein Pept Lett 32: 280-298, 2025.
14. Li J, Cao F, Yin HL, Huang ZJ, Lin ZT, Mao N, Sun B and Wang G: Ferroptosis: Past, present and future. Cell Death Dis 11: 88, 2020.
15. Zheng X, Jin X, Ye F, Liu X, Yu B, Li Z, Zhao T, Chen W, Liu X, Di C and Li Q: Ferroptosis: A novel regulated cell death participating in cellular stress response, radiotherapy, and immunotherapy. Exp Hematol Oncol 12: 65, 2023.
16. Noè R, Inglese N, Romani P, Serafini T, Paoli C, Calciolari B, Fantuz M, Zamborlin A, Surdo NC, Spada V, *et al*: Organic selenium induces ferroptosis in pancreatic cancer cells. Redox Biol 68: 102962, 2023.
17. Lei G, Zhang Y, Koppula P, Liu X, Zhang J, Lin SH, Ajani JA, Xiao Q, Liao Z, Wang H and Gan B: The role of ferroptosis in ionizing radiation-induced cell death and tumor suppression. Cell Res 30: 146-162, 2020.
18. Yang C, Dong Q, Bao H, Ge Y, Xu Z, Li J, Jiang X, Xu Y and Zhong X: Ferroptosis: New strategies and ideas for the treatment of pancreatic ductal adenocarcinoma. Front Biosci (Landmark Ed) 29: 45, 2024.
19. Zhang L, Yang L, Du K and Yang Y: Myoglobin improves doxycycline sensitivity in pancreatic cancer through promoting heme oxygenase-1-mediated ferroptosis. Environ Toxicol 39: 2166-2181, 2024.
20. Zhao X, Wang X, Zhang W, Tian T, Zhang J, Wang J, Wei W, Guo Z, Zhao J and Wang X: A ferroptosis-inducing arsenene-iridium nanoplatform for synergistic immunotherapy in pancreatic cancer. Angew Chem Int Ed Engl 63: e202400829, 2024.
21. Zhou Y, Men L, Sun Y, Wei M and Fan X: Pharmacodynamic effects and molecular mechanisms of lignans from *Schisandra chinensis* turcz. (baill.), a current review. Eur J Pharmacol 892: 173796, 2021.

22. Gao Y, Wu S, Cong R, Xiao J and Ma F: Characterization of lignans in *Schisandra chinensis* oil with a single analysis process by UPLC-Q/TOF-MS. Chem Phys Lipids 218: 158-167, 2019.
23. Olas B: Cardioprotective potential of berries of *Schisandra chinensis* turcz. (baill.), their components and food products. Nutrients 15: 592, 2023.
24. Yan LS, Zhang SF, Luo G, Cheng BCY, Zhang C, Wang YW, Qiu XY, Zhou XH, Wang QG, Song XL, *et al*: Schisandrin B mitigates hepatic steatosis and promotes fatty acid oxidation by inducing autophagy through AMPK/mTOR signaling pathway. Metabolism 131: 155200, 2022.
25. Lee TH, Jung CH and Lee DH: Neuroprotective effects of schisandrin B against transient focal cerebral ischemia in sprague-dawley rats. Food Chem Toxicol 50: 4239-4245, 2012.
26. Li J, Lu Y, Wang D, Quan F, Chen X, Sun R, Zhao S, Yang Z, Tao W, Ding D, *et al*: Schisandrin B prevents ulcerative colitis and colitis-associated-cancer by activating focal adhesion kinase and influence on gut microbiota in an in vivo and in vitro model. Eur J Pharmacol 854: 9-21, 2019.
27. Nasser MI, Zhu S, Chen C, Zhao M, Huang H and Zhu P: A comprehensive review on schisandrin B and its biological properties. Oxid Med Cell Longev 2020: 2172740, 2020.
28. Song A, Ding T, Wei N, Yang J, Ma M, Zheng S and Jin H: Schisandrin B induces HepG2 cells pyroptosis by activating NK cells mediated anti-tumor immunity. Toxicol Appl Pharmacol 472: 116574, 2023.
29. Tan S, Zheng Z, Liu T, Yao X, Yu M and Ji Y: Schisandrin B induced ROS-mediated autophagy and Th1/TH2 imbalance via selenoproteins in Hepa1-6 cells. Front Immunol 13: 857069, 2022.
30. Sana-Eldine AO, Abdelgawad HM, Kotb NS and Shehata NI: The potential effect of schisandrin-B combination with panitumumab in wild-type and mutant colorectal cancer cell lines: Role of apoptosis and autophagy. J Biochem Mol Toxicol 37: e23324, 2023.
31. He L, Chen H, Qi Q, Wu N, Wang Y, Chen M, Feng Q, Dong B, Jin R and Jiang L: Schisandrin B suppresses gastric cancer cell growth and enhances the efficacy of chemotherapy drug 5-FU in vitro and in vivo. Eur J Pharmacol 920: 174823, 2022.
32. Yan C, Gao L, Qiu X and Deng C: Schisandrin B synergizes docetaxel-induced restriction of growth and invasion of cervical cancer cells in vitro and in vivo. Ann Transl Med 8: 1157, 2020.
33. Yan YH, Kong L, Lu YB, Li SY, Yan AW, Song YW, Huang ZH and Zhu HN: Inhibition of hepatocellular carcinoma progression by methotrexate-modified pH-sensitive sorafenib and schisandrin B micelles. Biomed Mater 20: 015022, 2025.
34. Morris GM, Huey R, Lindstrom W, Sanner MF, Belew RK, Goodsell DS and Olson AJ: AutoDock4 and AutoDockTools4: Automated docking with selective receptor flexibility. J Comput Chem 30: 2785-2791, 2009.
35. Conroy T, Desseigne F, Ychou M, Bouché O, Guimbaud R, Bécouarn Y, Adenis A, Raoul JL, Gourgou-Bourgade S, de la Fouchardière C, *et al*: FOLFIRINOX versus gemcitabine for metastatic pancreatic cancer. N Engl J Med 364: 1817-1825, 2011.
36. Kim A, Ha J, Kim J, Cho Y, Ahn J, Cheon C, Kim SH, Ko SG and Kim B: Natural products for pancreatic cancer treatment: From traditional medicine to modern drug discovery. Nutrients 13: 3801, 2021.
37. Sahu SK, Prabhakar PK and Vyas M: Therapeutical potential of natural products in treatment of pancreatic cancer: A review. Mol Biol Rep 52: 179, 2025.
38. Jiang B, Yang J, Huang Q, Li W, Peng Q, Gan H, Peng T, Yao L and Qi L: Schisandrin B downregulates exosomal fibronectin 1 expression to inhibit hepatocellular carcinoma growth. Front Pharmacol 16: 1547685, 2025.
39. Dixon SJ, Lemberg KM, Lamprecht MR, Skouta R, Zaitsev EM, Gleason CE, Patel DN, Bauer AJ, Cantley AM, Yang WS, *et al*: Ferroptosis: An iron-dependent form of nonapoptotic cell death. Cell 149: 1060-1072, 2012.
40. Liu X, Yang J, Huang S, Hong Y, Zhu Y, Wang J, Wang Y, Liang T and Bai X: Pancreatic cancer-derived extracellular vesicles enhance chemoresistance by delivering KRASG12D protein to cancer-associated fibroblasts. Mol Ther 33: 1134-1153, 2025.
41. Zhao H, Huang Q, Liu YA and Wu W: Oncogenic KRAS promotes ferroptosis in pancreatic cancer through regulation of the Fosl1-tfrc axis. Pancreas 54: e235-e245, 2025.
42. Liu X, Peng X, Cen S, Yang C, Ma Z and Shi X: Wogonin induces ferroptosis in pancreatic cancer cells by inhibiting the Nrf2/GPX4 axis. Front Pharmacol 14: 1129662, 2023.
43. Xu M, Zhong W, Yang C, Liu M, Yuan X, Lu T, Li D, Zhang G, Liu H, Zeng Y, *et al*: Tiliroside disrupted iron homeostasis and induced ferroptosis via directly targeting calpain-2 in pancreatic cancer cells. Phytomedicine 127: 155392, 2024.
44. Liang X, Hu C, Han M, Liu C, Sun X, Yu K, Gu H and Zhang J: Solasonine inhibits pancreatic cancer progression with involvement of ferroptosis induction. Front Oncol 12: 834729, 2022.
45. Li J, Jia YC, Ding YX, Bai J, Cao F and Li F: The crosstalk between ferroptosis and mitochondrial dynamic regulatory networks. Int J Biol Sci 19: 2756-2771, 2023.
46. Chen X, Kang R, Kroemer G and Tang D: Broadening horizons: The role of ferroptosis in cancer. Nat Rev Clin Oncol 18: 280-296, 2021.
47. Chen F, Kang R, Liu J and Tang D: The ACSL4 network regulates cell death and autophagy in diseases. Biology (Basel) 12: 864, 2023.
48. Huang XD, Xiao FJ, Guo YT, Sun Y, Zhang YK and Shi XJ: Protein tyrosine phosphatase 1 protects human pancreatic cancer from erastin-induced ferroptosis. Asian J Surg 45: 2214-2223, 2022.
49. Zhou X, Kong L, Zhang B, Xie S, Wang W and Chen G: DPP4 suppresses pancreatic cancer growth by enhancing ferroptosis sensitivity through stabilization of ACSL4. Cell Signal 143: 112446, 2026.
50. Uchihara D, Shimajiri S, Harada Y, Kumamoto K, Oe S, Miyagawa K, Nakamura K, Katafuchi E, Nuratdinova F, Honma Y, *et al*: Long-chain fatty acyl CoA synthetase 4 expression in pancreatic cancer: A marker for malignant lesions and prognostic indicator for recurrence. Diagn Pathol 20: 59, 2025.
51. Qi R, Bai Y, Li K, Liu N, Xu Y, Dal E, Wang Y, Lin R, Wang H, Liu Z, *et al*: Cancer-associated fibroblasts suppress ferroptosis and induce gemcitabine resistance in pancreatic cancer cells by secreting exosome-derived ACSL4-targeting miRNAs. Drug Resist Updat 68: 100960, 2023.
52. He Z, Zheng D, Li F, Chen L, Wu C, Zeng Z and Yu C: TMOD3 accelerated resistance to immunotherapy in KRAS-mutated pancreatic cancer through promoting autophagy-dependent degradation of ASCL4. Drug Resist Updat 78: 101171, 2025.
53. Lei G, Zhuang L and Gan B: Targeting ferroptosis as a vulnerability in cancer. Nat Rev Cancer 22: 381-396, 2022.
54. Wang Y and Kanneganti TD: From pyroptosis, apoptosis and necroptosis to PANoptosis: A mechanistic compendium of programmed cell death pathways. Comput Struct Biotechnol J 19: 4641-4657, 2021.
55. Wang S, He H, Qu L, Shen Q and Dai Y: Dual roles of inflammatory programmed cell death in cancer: Insights into pyroptosis and necroptosis. Front Pharmacol 15: 1446486, 2024.
56. Strippoli A, Cocomazzi A, Basso M, Cenci T, Ricci R, Pierconti F, Cassano A, Fiorentino V, Barone C, Bria E, *et al*: c-MYC expression is a possible keystone in the colorectal cancer resistance to EGFR inhibitors. Cancers (Basel) 12: 638, 2020.
57. Yun CW and Lee SH: The roles of autophagy in cancer. Int J Mol Sci 19: 3466, 2018.
58. Santana-Codina N, Mancias JD and Kimmelman AC: The role of autophagy in cancer. Annu Rev Cancer Biol 1: 19-39, 2017.
59. Pizzimenti C, Fiorentino V, Ruggeri C, Franchina M, Ercoli A, Tuccari G and Ieni A: Autophagy involvement in non-neoplastic and neoplastic endometrial pathology: The state of the art with a focus on carcinoma. Int J Mol Sci 25: 12118, 2024.
60. Pizzimenti C, Fiorentino V, Franchina M, Martini M, Giuffrè G, Lentini M, Silvestris N, Di Pietro M, Fadda G, Tuccari G,and Ieni A: Autophagic-related proteins in brain gliomas: Role, mechanisms, and targeting agents. Cancers (Basel) 15: 2622, 2023.
61. Sorino J, Della Mura M, Ingravallo G, Cazzato G, Pizzimenti C, Zuccalà V, Pepe L, Germanà E, Martini M, Ieni A and Fiorentino V: *Fusobacterium nucleatum* and gastric cancer: An emerging connection. Int J Mol Sci 26: 7915, 2025.
62. Wang Z, You L, Cheng Y, Hu K, Wang Z, Cheng Y, Yang J, Yang Y and Wang G: Investigation of pharmacokinetics, tissue distribution and excretion of schisandrin B in rats by HPLC-MS/MS. Biomed Chromatogr 32: e4069, 2018.
63. Li S, Shao Q and Qiao H: Preclinical concomitant toxicokinetic study of schisandrin B by HPLC-MS/MS. Biomed Chromatogr 39: e70068, 2025.
64. Lee PK, Co VA, Yang Y, Wan MLY, El-Nezami H and Zhao D: Bioavailability and interactions of schisandrin B with 5-fluorouracil in a xenograft mouse model of colorectal cancer. Food Chem 463: 141371, 2025.